Modeling the metabolic interplay between a parasitic worm and its bacterial endosymbiont allows the identification of novel drug targets

DM Curran[1,*], A Grote[2,*], N Nursimulu[1,3], A Geber[2], D Voronin[4], Drew Jones[5], E Ghedin[2,6,#], J Parkinson[1,3,7,8,#]

* These authors contributed equally to this work

Co-corresponding authors

[1]Program in Molecular Medicine, Hospital for Sick Children, Toronto, ON, Canada

[2]Department of Biology, Center for Genomics & Systems Biology, New York University, New York, NY, USA

[3]Department of Computer Science, University of Toronto, Toronto, ON, Canada

[4]New York Blood Center, New York, NY, USA

[4]Department of Biochemistry and Molecular Pharmacology, New York University School of Medicine, New York, NY, USA

[5]Department of Epidemiology, College of Global Public Health, New York University, New York, NY, USA

[7]Department of Biochemistry, University of Toronto, Toronto, ON, Canada

[8]Department of Molecular Genetics, University of Toronto, Toronto, ON, Canada

Keywords: Metabolic reconstruction, Flux Balance Analysis, *Brugia malayi*, *Wolbachia*, metabolomics

Abstract

The filarial nematode *Brugia malayi* represents a leading cause of disability in the developing world, causing lymphatic filariasis in nearly 40 million people. Currently available drugs are not well-suited to mass drug administration efforts, so new treatments are urgently required. One potential vulnerability is the endosymbiotic bacteria *Wolbachia*—present in many filariae—which is vital to the worm.

Genome scale metabolic networks have been used to study prokaryotes and protists and have proven valuable in identifying therapeutic targets, but only recently have been applied to eukaryotic organisms. Here, we present *i*DC625, the first compartmentalized metabolic model of a parasitic worm. We used this model to show how metabolic pathway usage allows the worm to adapt to different environments, and predict a set of 99 reactions essential to the survival of *B. malayi*. We validated three of those reactions with drug tests and demonstrated novel antifilarial properties for all three compounds.

INTRODUCTION

Filarial nematodes are responsible for neglected tropical parasitic diseases that are among the leading causes of morbidity worldwide. One of the most debilitating is lymphatic filariasis (LF)—also called elephantiasis—which is caused by *Brugia malayi, Brugia timori*, and *Wuchereria bancrofti*. As of 2015, an estimated 38.8 million people had lymphatic filariasis with an estimated 1 billion people at risk in 72 endemic countries (Vos *et al.*, 2016). Transmission occurs when microfilariae released by a female worm within an infected individual circulate in the blood where they are ingested by one of several species of mosquito. In the insect vector, the larvae undergo development; during subsequent blood meals, they are transmitted to a mammalian host where the L3 larvae complete their development into adults (Gleave *et al.*, 2016).

Current mass drug administration efforts involve a small selection of drugs—diethylcarbamazine, ivermectin, and albendazole—with limited effectiveness against the adult stages of the parasites. To prevent transmission and to relieve symptoms, treatment must continue for the lifespan of the adult worms, which can be up to 15 years (Molyneux *et al.*, 2014). Furthermore, diethylcarbamazine is contraindicated in regions where *Onchocerca volvulus* or *Loa loa*—other filarial nematodes—are endemic (Gyapong *et al.*, 2005; Taylor *et al.*, 2010). Ivermectin is also contraindicated in regions where *L. loa* is co-endemic due to potential life-threatening complications (Gardon *et al.*, 1997; Boussinesq *et al.*, 1998, 2006). While anthelmintic resistance has not yet manifested as a serious treatment issue in humans as it has in veterinary medicine (Kaplan and Vidyashankar, 2012), the potential remains a serious threat; emergence of resistance in these species against diethylcarbamazine (Eberhard *et al.*, 1991), ivermectin (Awadzi *et al.*, 2004; Eng *et al.*, 2006), and albendazole (Schwab *et al.*, 2005) has been reported for many years.

An alternative strategy for treatment has been the use of traditional antibiotics to target the endosymbiotic bacteria that live within most filarial nematodes. These bacteria are from the genus *Wolbachia*, specific to each helminth, and found to be essential for adult worm fitness and reproduction (Taylor *et al.*, 2013). Targeting these bacteria with the antibiotic doxycycline was shown to reduce numbers of *Wolbachia* present in the

worms, sterilize adult females, and reduce symptoms of lymphatic filariasis (Debrah *et al.*, 2009; Rao *et al.*, 2012; Ghedin *et al.*, 2009; Taylor *et al.*, 2010). While antibiotic treatment remains a viable option for individual patients, long treatment times and contraindications for children and pregnant women limit its suitability for mass-drug administration efforts (Taylor *et al.*, 2010). This strategy is ongoing, as recent evidence suggests that the commonly used antibiotic rifampicin may also possess filaricidal activity, but these data are preliminary and have not yet been tested in humans (Aljayyoussi *et al.*, 2017). A more recent study proposes faster-acting antibiotics that belong to the tetracycline class of drugs (Taylor *et al.*, 2019).

Considering the limitations of current treatment regimes, there is an urgent need to identify new drug targets against filarial nematodes that directly impact adult worm survival and, if possible, are specific enough to avoid the potential complications that arise in regions co-endemic for *O. volvulus* or *L. loa*. Genome scale metabolic reconstruction and constraint-based modelling have emerged as effective strategies to identify critical metabolic enzymes and pathways (Oberhardt *et al.*, 2008; Chavali *et al.*, 2008; Lee *et al.*, 2009; Song *et al.*, 2013), which, due to their importance in energy production and in generating the building blocks required for growth and survival, are good potential therapeutic targets (Cotton *et al.*, 2016; Chiappino-Pepe *et al.*, 2017). These models can be analyzed using flux balance analysis (FBA), an optimization method that is applied to a metabolic network (reviewed in (Orth *et al.*, 2010)). Briefly, it calculates the maximum amount of biomass that can be produced given the available nutrients and the reaction constraints in the model, as well as the flux through each reaction needed to attain that solution.

Here, we describe the first metabolic reconstruction and constraint-based models of *B. malayi*. Using the high quality genome sequence of *B. malayi* (Ghedin et al., 2007), we first generated a network representation of the parasite's metabolic capabilities. Integrating previously published stage-specific transcriptome datasets for both *B. malayi* and its *Wolbachia* endsymbiont (Grote et al., 2017), we revealed stage-specific metabolic dependencies and identified enzymes that are predicted to be effective targets for drug intervention strategies. In subsequent drug inhibition studies, we

validated three of these targets and show the novel antifilarial properties of three human drugs. To our knowledge, this work represents the first compartmentalized metabolic model for any parasitic nematode.

RESULTS

*i*DC625: The first genome scale metabolic model for *B. malayi*

To develop a genome scale metabolic model of *B. malayi*, we first used as a scaffold network a set of enzymes that are homologs of *O. volvulus* and part of a previously generated metabolic reconstruction for that organism (Cotton *et al.*, 2016). The *B. malayi* network was then manually curated to ensure that the major pathways—such as the TCA cycle, fatty acid metabolism, and anaerobic metabolism—were complete and could be used by the model. The model was divided into three compartments representing the cytosol and mitochondria of *B. malayi*, as well as the *Wolbachia* endosymbiont. Where orthologous relationships could be inferred, *B. malayi* reactions were assigned to either the cytosol or mitochondrion on the basis of similar designations in the *i*CEL1273 metabolic model for *Caenorhabditis elegans* (Safak Yilmaz and Walhout, 2016). Additional compartment assignments were performed with reference to literature sources. In the absence of such information, reactions were split into both cytosolic and mitochondrial forms. Metabolites were confined to a single compartment, and so they could only participate in reactions in other compartments if shuttled there by an explicit transport reaction. Most of these transporters were taken from the *i*CEL1273 model, except when contraindicated by (Berg *et al.*, 2002). Since *Wolbachia* lacks the genes necessary to produce NAD+, coenzyme A (CoA), ubiquinol, and folate (Voronin *et al.*, 2016), reactions were added to allow the transport of each metabolite into the *Wolbachia* compartment from the cytosol.

In order to model *B. malayi* growth with pFBA (parsimonious FBA), we assembled a set of required biomass metabolites together with their relative abundances. This collection represents the biomass objective function and is used in constraints-based modeling to calculate flux distributions for each reaction in the reconstruction. Here we based the objective function on a previously defined function generated for *O. volvulus* (Cotton *et al.*, 2016; see Supplemental Methods for details), modified with *B. malayi* and *Wolbachia* specific values for DNA, RNA and amino acid distributions that were

obtained from previously published studies (Ghedin *et al.*, 2007; Foster *et al.*, 2005; Grote *et al.*, 2017).

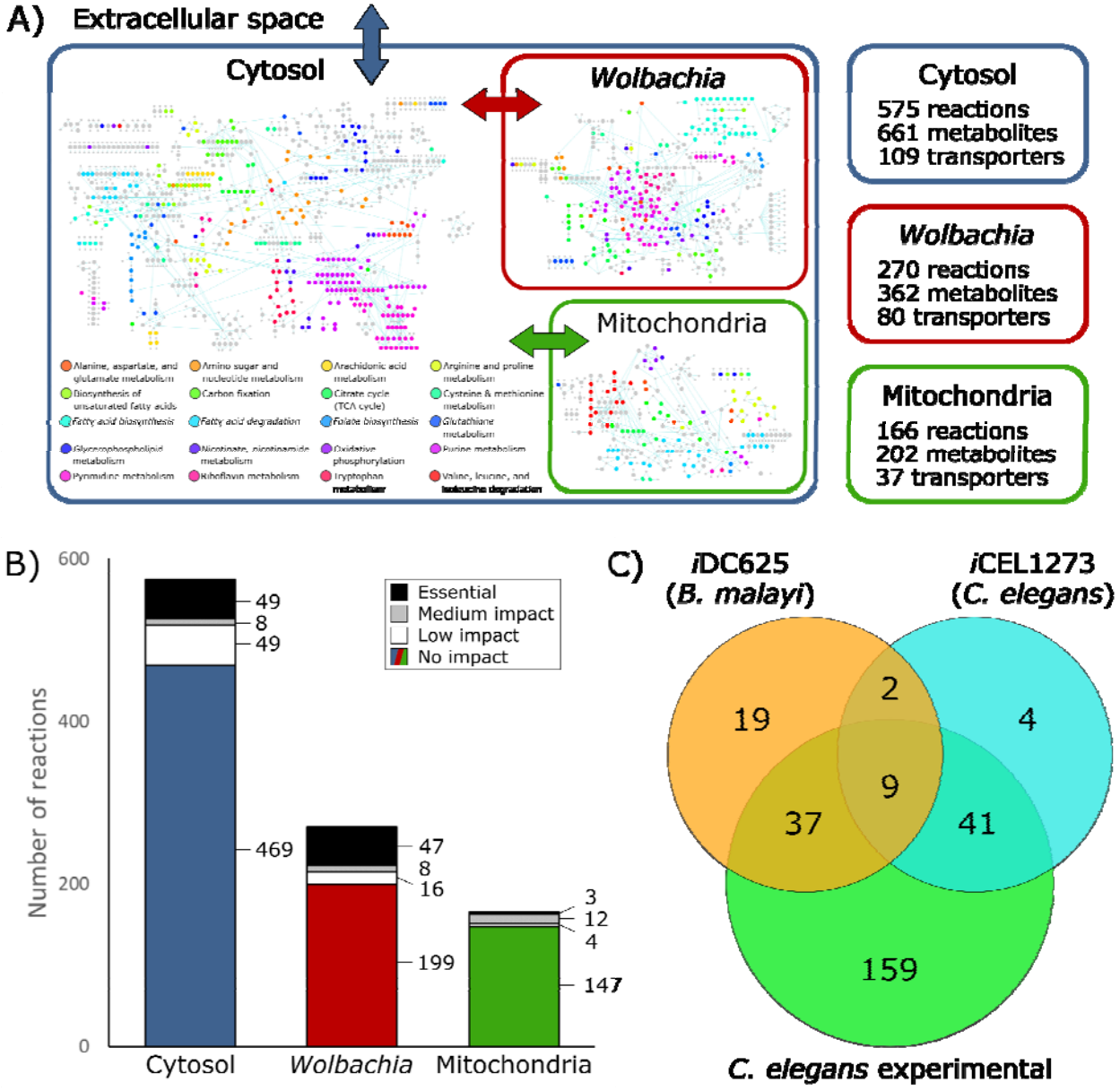

Figure 1. The *i*DC625 genome scale metabolic model. A) Network representation of our metabolic reconstruction, where the large coloured dots represent reactions. B) Breakdown of the essentiality of the model reactions by their compartment. No impact indicates the model's optimized biomass objective function was unaffected; low impact indicates 100% > biomass > 90% of the original; medium impact indicates 90% ≥ biomass > 0%; and essential indicates that no biomass was produced. C) A Venn

diagram of the overlap in predicted essential reactions between our model, the previously published *i*CEL1273 *C. elegans* metabolic reconstruction, and experimentally determined essential reactions in *C. elegans*. All three sets of reactions represent only those that are present in both *i*DC625 and *i*CEL1273.

The final reconstruction, designated *i*DC625, contains 1,266 total reactions involving 1,252 total metabolites. Of the 1,266 reactions, 1,011 represent enzymes of which 849 are associated with 625 genes; 575 of these enzymatic reactions are associated with the cytosolic compartment, 166 with the mitochondria, and 270 with *Wolbachia* (**Figure 1**). Of the remaining reactions, 226 are associated with transport across compartments, of which 37 represent metabolite exchange between the mitochondria and cytosol, 80 between *Wolbachia* and the cytosol, and the remaining 109 representing metabolite exchange between the cytosol and the extracellular milieu. A further 29 reactions are artificial, used only to organize the biomass components required for the objective function. Of the 1,252 metabolites, 661 are associated with the cytosol, 202 with the mitochondrion, 362 with the *Wolbachia*, and 27 are used in the artificial conversions of biomass components.

We also used life stage-specific gene expression data to constrain the reactions of *i*DC625. In total, we obtained relative expression data for 11,840 *B. malayi* and 823 *Wolbachia* genes across ten different points in the worm's lifecycle; 87.6% of the *B. malayi* genes and 96.4% of the *Wolbachia* genes were expressed in at least one stage. This yielded 11 total models: unconstrained (open), L3, L3 6 days post-infection (L3D6), L3 9 days post-infection (L3D9), L4, adult female 30 days post-infection (F30), adult female 42 days post-infection (F42), adult female 120 days post-infection (F120), adult male 30 days post-infection (M30), adult male 42 days post-infection (M42), and adult male 120 days post-infection (M120).

Wolbachia **load impacts model performance**

Since the presence of *Wolbachia* directly impacts model dynamics, both through the production of metabolites that contribute to the biomass objective function as well as the consumption of metabolites to maintain its own growth, the relative weight between bacteria and worm must be considered in the model. This weight is implemented by weighting the *Wolbachia* contribution to the biomass objective function, as well as constraining reactions assigned to the endosymbiont. Using these constraints in a pFBA framework, we examined how changes in *Wolbachia* populations affect the maximum flux through the objective function of the model. As the availability of a carbon source and of oxygen are two of the most important determinants of the model's activities, we examined the model under four different nutrient conditions: high oxygen (580 units) and high glucose (250 units) (HOHG), high oxygen and low glucose (45 units) (HOLG), low oxygen (90 units) and high glucose (LOHG), and low oxygen and low glucose (LOLG).

By applying these constraints to the otherwise unconstrained model and varying the relative load of *Wolbachia*, we found that the maximum production of the biomass objective function occurs at *Wolbachia* weights of 0.04, 0.02, 0.02, and 0.01 under HOHG, HOLG, LOHG, and LOLG, respectively (**Figure 2**). Under all conditions the model was infeasible with no *Wolbachia* (which agrees with the experimentally determined essential role of the endosymbiont), and as the *Wolbachia* weight increased the objective function peaked rapidly followed by a steady decline. Since the negative impact to the objective function was minimal until 0.18, we assigned a weight of 0.1 under all nutrient conditions. This was chosen to minimize the impact on the objective function, while still being conservative in allowing reasonable flux through *Wolbachia* reactions.

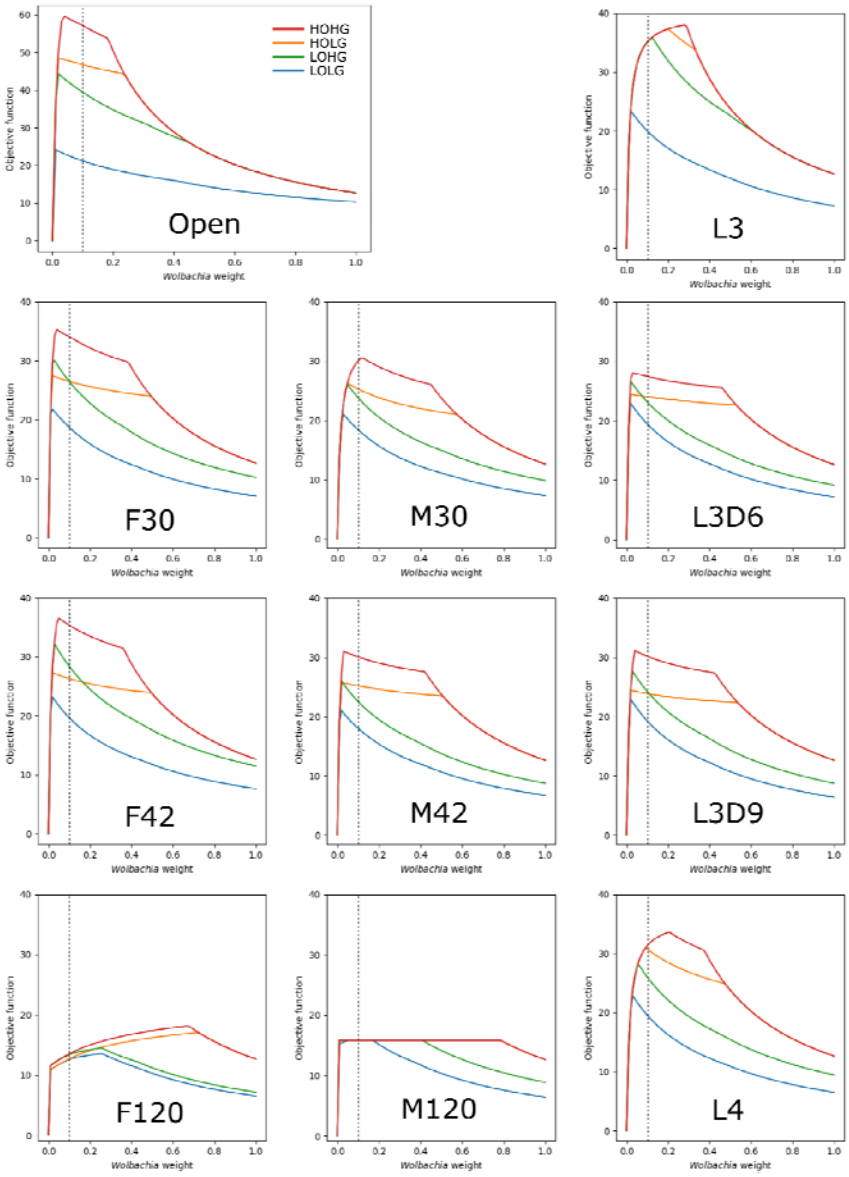

193

194 **Figure 2: The effect of the *Wolbachia* load on the maximum objective function flux**
195 **under different nutrient conditions and lifecycle stages.** The dashed line indicates
196 the *Wolbachia* weight of 0.1 used in all subsequent experiments.

197

198 The behavior of the other lifecycle models was relatively similar, except for F120 and
199 M120, which had by far the least metabolic activity. In all cases the models were more
200 sensitive to increasing the *Wolbachia* weight under low oxygen than under low glucose

conditions, as evidenced by the relative gradients associated with LOHG compared to HOLG (**Figure 2**).

Altering nutrient conditions reveals a metabolic landscape rich in alternative energy production pathways

Over the course of its lifecycle, *B. malayi* encounters a range of different nutrient conditions and likely regulates enzyme expression to alter metabolic flux to optimize growth in each condition. For example, adult worms are found in the lymphatic system where the expectation is that the parasite is exposed to a substantially lower oxygen environment compared to other life stages. We therefore performed a series of pFBA simulations in which we examined the impact of changes in two key metabolites on worm growth, oxygen and glucose, in the different lifecycle models (**Figure 3**). Fumarase is one of the measured reactions and is part of the TCA cycle that converts fumarate into malate. In addition to being located directly downstream of Complex II in the TCA cycle, it is also directly upstream of the anaerobic reverse Complex II (**Figure 4**). Given that fumarase is reversible, flux measurements provide an indication of the activity of both aerobic and anaerobic metabolism. As expected, pFBA predicts a reliance on anaerobic pathways under low oxygen conditions (**Figure 3**). However, at an oxygen concentration of 205 flux units (**Figure 3**, *vertical dashed line*), there is a switch to the aerobic pathway in the unconstrained and L3 models. Interestingly, the acetate and propanoate waste transporters are no longer used above this threshold; the predicted presence of these waste products is consistent with previous studies of helminth anaerobic metabolism (Tielens *et al.*, 2010; Muller *et al.*, 2012).

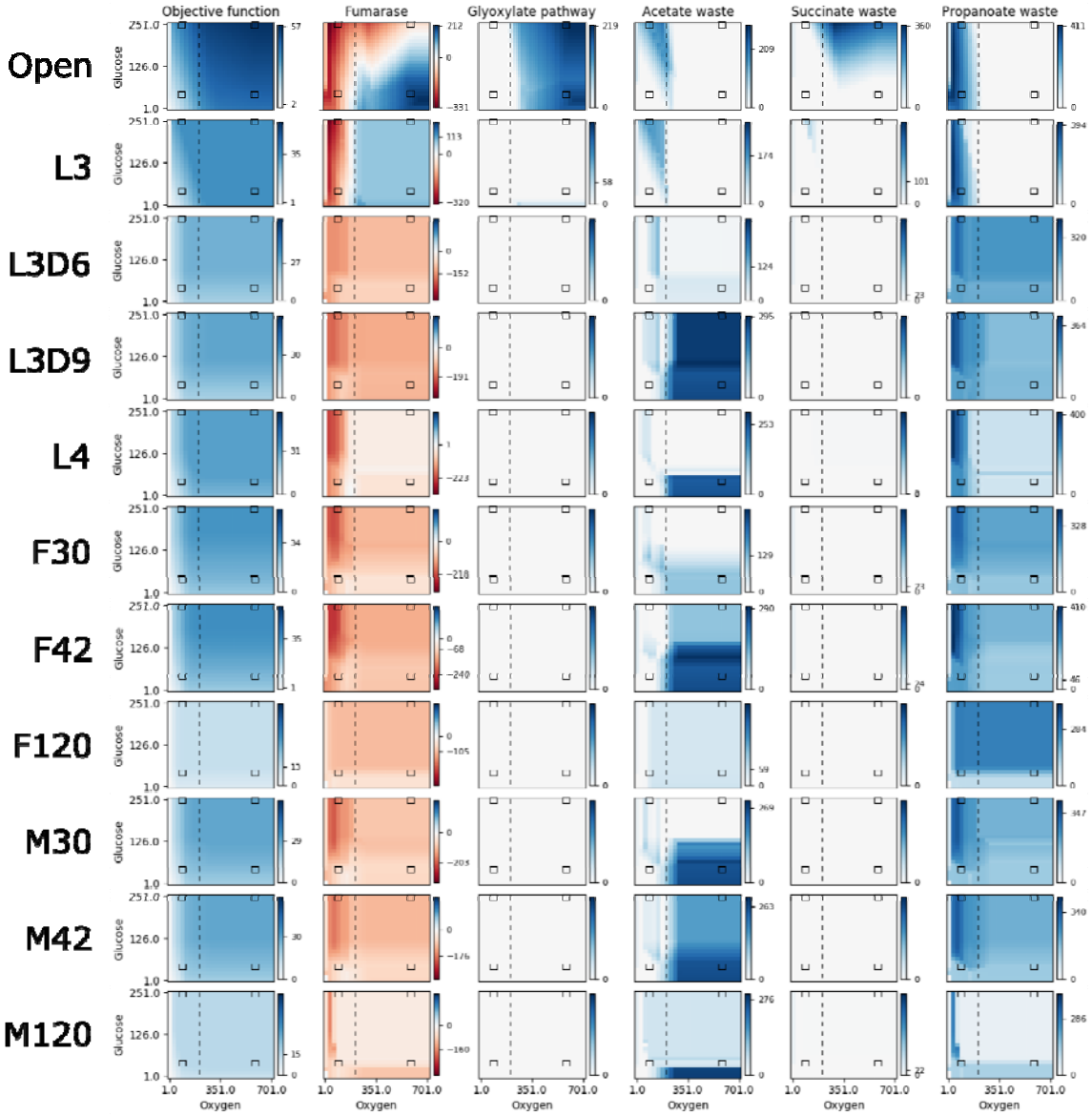

Figure 3. Reaction fluxes when varying oxygen and glucose. The activities of the objective function and five other reactions are shown for a range of 25 oxygen and 25 glucose availabilities, for each lifecycle model. For each, pFBA was performed for all 625 combinations of oxygen and glucose; the colour of each pixel in the heatmap indicates the activity of the reaction at that nutrient availability, with white, dark blue, and dark red indicating no activity, maximum forward, and maximum reverse, respectively. As each reaction has a different activity profile, each has its own colour legend. The four black boxes on each graph indicate what we discuss as low and high concentrations of

233 oxygen (90 / 580) and glucose (45 / 250), and the vertical dashed line indicates the
234 anaerobic-aerobic threshold at 205 units of oxygen.

235

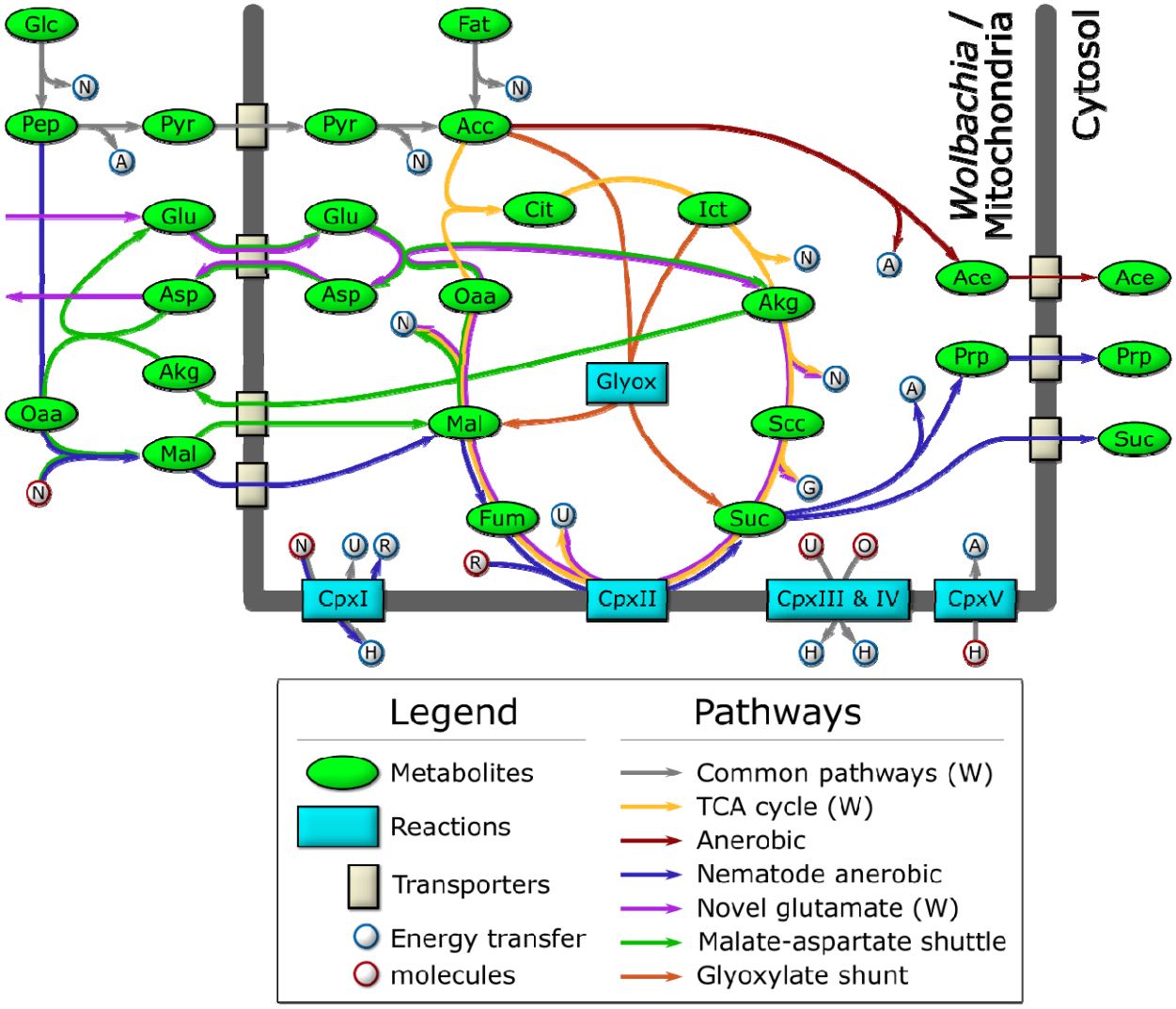

236

237 **Figure 4. Schematic diagram of the major catabolic pathways observed in the**
238 **model.** Metabolites were manually tracked in the model under many different nutrient
239 conditions and lifecycle expression constraints, and the major catabolic pathways are
240 diagrammed here. The thick dark line indicates the mitochondrial / *Wolbachia*
241 membrane, and those pathways present in, or feeding into, the *Wolbachia* compartment
242 are indicated by (W). The labeled metabolites are Glc: glucose; Pep:
243 phosphoenolpyruvate; Pyr: pyruvate; Acc: acetyl-coenzyme A; Fat: fatty acids; Cit:

citrate; Ict: isocitrate; Akg: alpha-ketoglutarate; Scc: succinyl-coenzyme A; Suc: succinate; Fum: fumarate; Mal: malate; Oaa: oxaloacetate; Glu: glutamate; Asp: aspartate; Ace: acetate; Prp: propanoate. The labeled reactions are CpxI: Complex 1; CpxII: Complex 2; CpxIII: Complex 3; CpxIV: Complex 4; CpxV: Complex 5; Glyox: glyoxylate. The energy transfer molecules are common metabolites, where a blue border indicates that the molecule was produced, and a red border indicates that it was consumed. The labeled energy transfer molecules are A: ATP; G: GTP; N: NADH; U: ubiquinol; R: rhodoquinol; H: proton-motive force; O: oxygen.

To further explore the impact of glucose and oxygen availability on *B. malayi* metabolism, we conducted detailed analyses under the four diverse nutrient conditions previously described: HOHG, HOLG, LOHG, and LOLG. For each condition, the model was provided with sufficient fatty acids (50 units), amino acids (100 units), and several cofactors: ammonia, phosphate, H^+, adenine, pyridoxal phosphate, heme, folate, cholesterol, oleic acid, pantothenate, choline, riboflavin, putrescine, nicotinate, UTP, CTP, $Fe2^+$, and N-acetyl-D-glucosamine; in all simulations, the maximum usage of fatty acids, amino acids, and cofactors was less than was provided.

We observe that the model produces the most biomass under HOHG conditions, as expected. Instead of using the full TCA cycle, the model predicts a reliance on the glyoxylate shunt to produce malate and succinate (**Figure 4**). A large proportion (74.6%) of malate is processed by the TCA cycle to isocitrate which is recycled back into the glyoxylate shunt, and 18.2% is predicted to be processed through anaerobic pathways to produce succinate, a phenomenon termed the Crabtree effect (Postma *et al.*, 1989; Pfeiffer and Morley, 2014), in which anaerobic pathways are used by the cell in the presence of high oxygen and glucose. Succinate produced through both pathways is subsequently exported from the cell as waste. The majority of the oxygen imported (74.5%) is used to generate ATP through oxidative phosphorylation, while only 6.2% (36 units) is predicted to be used by *Wolbachia*.

Under HOLG conditions, growth is predicted to fall to 82% of optimal biomass production. While the glyoxylate shunt is still used, succinate is no longer exported, but

instead is processed by the TCA cycle to produce energy, with CO_2 subsequently exported as waste. Similar to HOHG, 71.2% of the oxygen is used for oxidative phosphorylation in the mitochondria, while 6.0% (35 units) is used by *Wolbachia*.

Under LOHG conditions, biomass production falls to 69%. Here, the glycolytic pathway is used to generate energy, with glucose metabolized to phosphoenolpyruvate (PEP) producing approximately half of the total NADH used by the model, which is then transported into the mitochondria via the malate-aspartate shuttle. The other half of the NADH is produced by the classical anaerobic pathway involving the conversion of some PEP (37.3%) to pyruvate, which is subsequently transported into the mitochondria, metabolized to acetate, and excreted as waste. However, most of the PEP (59.0%) is processed by the nematode-specific anaerobic pathway. Through this pathway, PEP is metabolized into malate and transported to the mitochondria where it is processed to succinate by the reverse Complex II, and ultimately converted to propanoate and exported as waste. Under these conditions, most of the oxygen in the model (61.0%) is used to generate ATP through oxidative phosphorylation, while 37.8% (34 units) is used by *Wolbachia*.

Under LOLG conditions biomass production is reduced to 37% of the optimal. Glucose is converted to malate and transported into the mitochondria as observed under LOHG conditions. Approximately half is processed to succinate by the reverse Complex II, while the other half is used to generate NADH via conversion to oxaloacetate, α-ketoglutarate (AKG), succinyl-CoA, and then succinate. All of the succinate is then converted to propanoate and exported. Under these conditions 69.8% of the oxygen is being consumed by oxidative phosphorylation, and 29.6% (27 units) is used by *Wolbachia*.

Interestingly, the model predicts a potentially novel form of glutamate metabolism, representing a combination of the malate-aspartate shuttle and the tricarboxylic acid (TCA) cycle (**Figure 4**). It is similar to the utilization of malate under LOLG conditions, except that succinate is recycled by the TCA cycle instead of being exported. In this pathway, glutamate is first transported into the mitochondria in exchange for aspartate, before combining with oxaloacetate to yield AKG and aspartate. AKG is then processed

by the TCA cycle to regenerate oxaloacetate. The net reaction results in the conversion of glutamate to aspartate and CO_2, along with the production of key energy metabolites: GTP, 2 x NADH, and ubiquinone. This is almost equivalent to the energy produced by the catabolism of a single molecule of acetyl CoA by the TCA cycle: 2 x CO_2, GTP, 3 x NADH, and ubiquinone. However, given that the glutamate/aspartate transporter is driven by the proton-motive force, which is not specifically modeled by pFBA, it is not known if this pathway would be energetically favourable *in vivo* (Bremer and Davis, 1975; Bakker *et al.*, 2001) and so may therefore not be physiologically relevant.

It has previously been suggested that *Wolbachia* may function to supplement mitochondrial energy production in filarial nematodes (Darby *et al.*, 2012); our model predictions support this hypothesis. Under LOLG conditions, *Wolbachia* is predicted to export the maximum amount of ATP possible (100 units) into the *B. malayi* cytosol. It was also suggested that *Wolbachia* uses pyruvate as its primary carbon source (Voronin *et al.*, 2016), but under LOLG conditions pyruvate import is nearly zero, and *Wolbachia* is using the novel glutamate metabolic pathway described above. Under LOHG conditions, *Wolbachia* ATP export drops to 90% compared to LOLG conditions. Pyruvate import increases substantially (9 units instead of 1), and the model uses both the TCA cycle and the glutamate metabolic pathway to generate energy. The *Wolbachia* metabolic pathways appear much the same under the other conditions, except that ATP export drops to 71%, and 44% of LOLG for HOLG and HOHG, respectively.

Lifecycle stage specific metabolic models of *B. malayi* reveal a dynamic reliance on alternative pathways

To determine how metabolic pathway dependencies may vary across the *B. malayi* life cycle, pFBA was performed under the four different nutrient conditions for each of the ten lifecycle stages (**Figure 5**). As expected, the models produced the most biomass under HOHG conditions, and the unconstrained (open) model produced the most under all conditions. In general, models are able to produce more biomass when presented with additional nutrients, which is why biomass production increases when moving from low glucose to high glucose, under both low and high oxygen conditions (LOLG to

334 LOHG or HOLG to HOHG). There was little difference in model performance under
335 LOLG conditions, except for adult worms at 120 dpi (M120 and F120). This indicates
336 that the different reaction constraints are playing a minor role in this scenario, and that
337 the concentrations of glucose and oxygen are the limiting factors for adult worms.

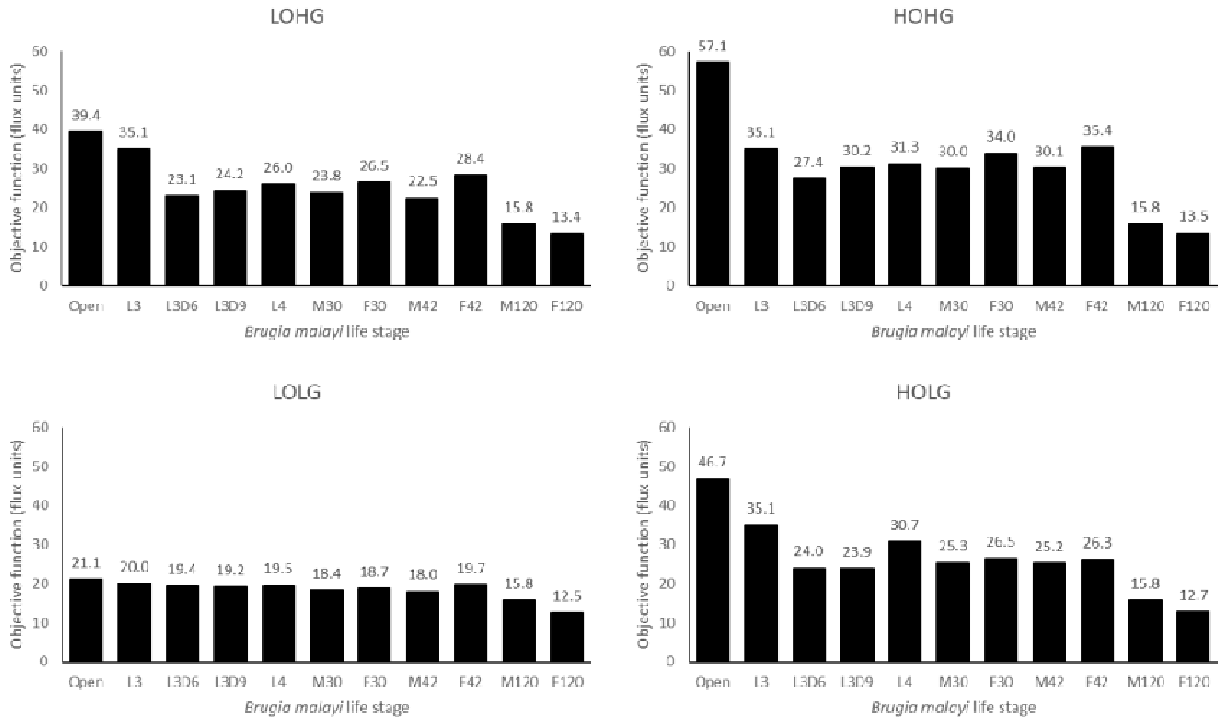

338

339 **Figure 5. Biomass production across lifecycle stages under different nutrient**
340 **conditions.** The maximum biomass produced by each model under LOLG, LOHG,
341 HOLG, and HOHG conditions.

342

343 While the L3 model experiences a large benefit from LOHG or HOLG compared to
344 LOLG, there is no increased benefit under HOHG conditions. This indicates that the
345 reaction constraints imposed for this stage limit the model's ability to exploit increases in
346 these metabolites. Similarly, the M120 model also appears saturated for these
347 metabolites, even under LOLG conditions, while the F120 model receives only a modest
348 benefit from additional glucose or oxygen.

Besides measuring the biomass production for each model under different nutrient conditions, we also quantified the number of reactions used by the models (**Figure 6**). We found that the *Wolbachia* compartment changes the least among the different models and conditions, while the mitochondrial compartment shows the most variation. This also allows us to identify "enzymatically constrained" models, which is a term that relates to the number of possible ways a model is able to achieve its maximum objective flux; if there are multiple alternate metabolic pathways that can be used to satisfy the objective function, a model would be considered enzymatically unconstrained. Models generally become less constrained as they are provided with more nutrients.

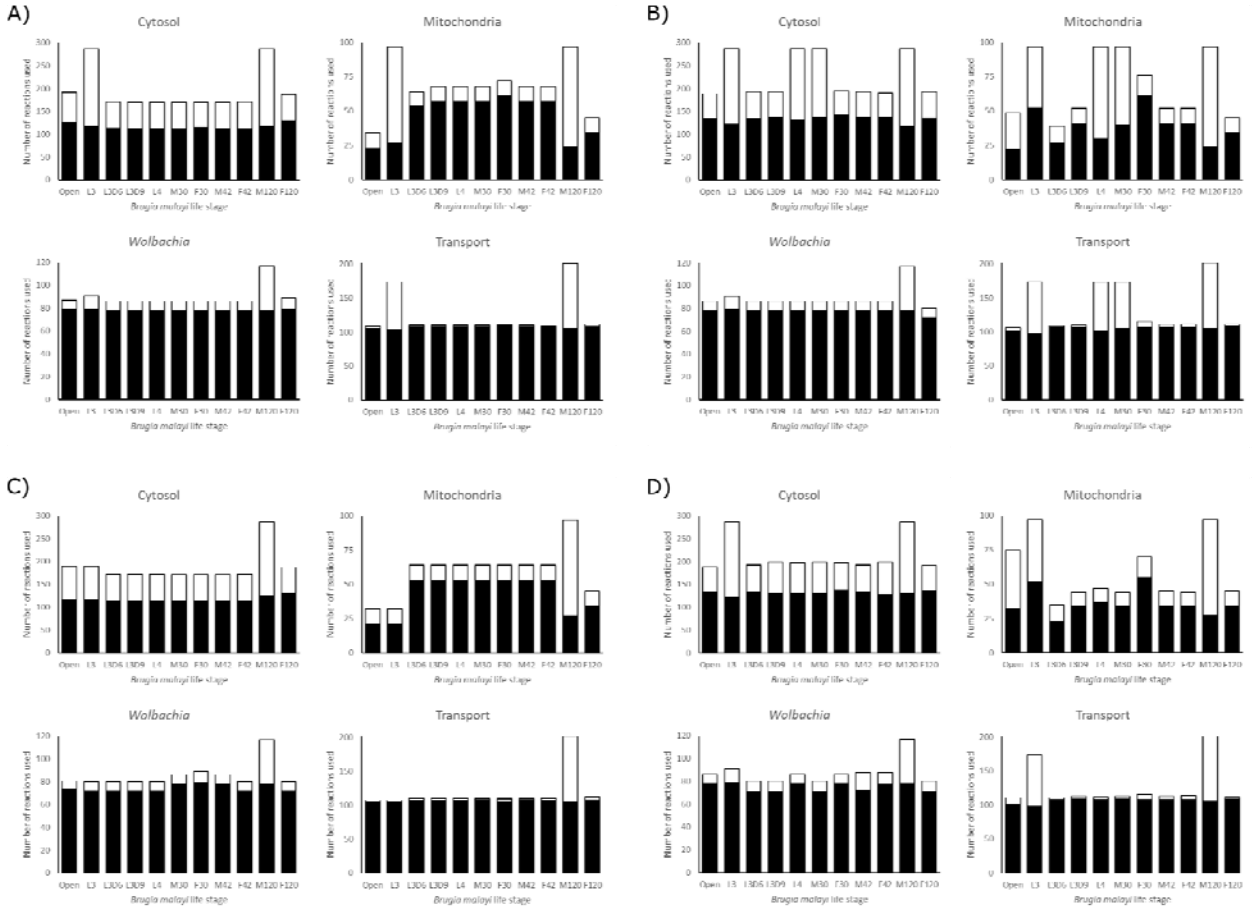

Figure 6. Reaction utilization across lifecycle stages. The number of reactions used by each model in each compartment to achieve its maximum objective function flux, under A) LOHG, B) HOHG, C) LOLG, and D) HOLG conditions. The black bars indicate

363 the number of reactions used in the most parsimonious solution, while the stacked white
364 bars indicate the number of reactions used in all possible solutions that yield the same
365 value for the objective function. The larger the height discrepancy between the two bars,
366 the more redundant pathways the model has to achieve the same objective function
367 flux.

368

369 It is interesting to note that both the L3D6 and L3D9 models appear to be substantially
370 more enzymatically constrained than L3. These two models represent the time when *B.*
371 *malayi* is molting, specifically during the apolysis stage of molting where a new cuticle is
372 being synthesized to replace the old cuticle. These reduced usage numbers, combined
373 with reduced biomass production (**Figure 5**), may reflect this specialized function and
374 large energetic expenditure. Differences between these related models extend to
375 pathway utilization as well. Under HOHG conditions, the L3 model uses the whole TCA
376 cycle—though fatty acids are used as the sole carbon source instead of glucose—while
377 the other two models exhibit the apparent Crabtree effect. Unlike the unconstrained
378 model, none of these three larval-stage models export any significant amount of
379 succinate. Additional differences include L3D9 exporting a large quantity of acetate, and
380 L3D6 and L3D9 exporting propanoate.

381

382 **Metabolomics data identify intermediates throughout, but lowest in L3**

383 To help validate our reconstruction, we performed untargeted metabolomics on worm
384 extracts from four different lifecycle stages. Applying two complementary approaches,
385 our analyses identified 146 unique metabolites from a ‘hybrid’ analysis and 492 from a
386 ‘predictive’ analysis (see Supplementary information for details); of these, 103 and 316
387 metabolites were found in at least three samples, respectively. Directly relating these
388 data to the model predictions is unfortunately non-trivial, as the metabolomics analyses
389 detect the size of the pool of some metabolite at one point in time, while our pFBA
390 predictions are steady-state rates.

Most of the TCA cycle intermediates (**Figure 4**) were detected in one or both of our metabolomics data sets. Phosphoenolpyruvate was only detected in adults in the hybrid analysis but was found in the microfilaria and L3 stages as well as in the predicted analysis. Pyruvate was detected only in the adult worms in the hybrid analysis, and at the highest levels in males. Oxaloacetate was detected in all stages in the predicted analysis, but at the lowest levels in the adults. Citrate and isocitrate were detected in the adults and one microfilaria sample in the predicted analysis, and only in the adults in the hybrid analysis. Alpha-ketoglutarate was detected in both analyses in the adults and one microfilaria sample, highest in the females. Succinate, fumarate, and malate were detected in the adults and microfilaria, with none in the L3 samples. This pattern was consistent in both analyses, except for succinate which was missing from the hybrid analysis. No acetyl-CoA or succinyl-CoA were detected in either analysis.

We were able to detect several fatty acid degradation intermediates as well, in particular carnitine-conjugated fatty acids. Carnitine and acetylcarnitine were detected in all samples in both analyses and were found to be highest in males, followed by females, microfilaria, and finally L3. Other short-chain acylcarnitines, butyrylcarnitine and valerylcarnitine were detected in all samples except L3 in the hybrid analysis. Consistent with above, these metabolites were found to be highest in males, followed by females, and then microfilaria. Propionylcarnitine was detected only in the adult samples in the hybrid analysis. The only long-chain fatty acid intermediate detected was palmitoylcarnitine, and only in the microfilaria and one male sample in the predicted analysis.

If we accept that higher levels of these intermediates imply increased metabolic activity, then we observe a general trend of the highest activity in the adults (in particular males metabolizing fatty acids), followed by the microfilaria, with L3 having the lowest levels if any were detected. This fits with the observation that L3 is a non-feeding stage, which has been likened to the dauer stage of *C. elegans* (Li *et al.*, 2009).

Modeling of *B. malayi* metabolism predicts novel therapeutic targets

To identify critical reactions in the metabolic network that represent potential therapeutic targets, we performed a series of *in silico* knockouts in which each reaction constraint was set to zero (i.e. no flux was allowed through that reaction). Of the 1,011 enzymatic reactions in *i*DC625, 815 had no impact on the biomass objective function when knocked out (**Figure 1B**); 69 were found to have a low impact (100% > biomass > 90% of original), 28 had a medium impact (90% ≥ biomass > 0%), and 99 were found to be essential (biomass = 0%). The biomass breakpoints for no impact and essential were actually set to within 0.0001 flux units (< 0.0002% of the biomass) of the true values to account for floating point errors.

This set of essential genes was compared to those predicted in the *i*CEL1273 *C. elegans* model, as well as experimentally determined essential reactions (Safak Yilmaz and Walhout, 2016). The authors used a more liberal definition of essential reactions, selecting all of those that reduced the model's biomass by 50% or more. They predicted 159 essential genes, corresponding to 125 KEGG reactions, 56 of which are also found in *i*DC625; of the 99 reactions we predict to be essential, 67 were found in the *i*CEL1273 model. They also list 461 *C. elegans* genes that have been experimentally determined to be essential; these correspond to 425 KEGG reactions, 246 of which are also found in *i*DC625. There were only 11 essential reactions shared by *i*CEL1273 and *i*DC625 (**Figure 1C**), but this low overlap is likely because both models are missing many true essential reactions. This is suggested by the large overlap between each model's predictions and the experimentally determined essential reactions; even though they are evolutionarily distinct species, 69% of the predicted *i*DC625 essential reactions overlap with the experimentally determined essential reactions of *C. elegans*.

In addition to single reactions, we also investigated reaction pairs exhibiting synthetic lethal relationships. Such relationships may exist, for example, when two reactions operate in alternative pathways that can each lead to production of the same key metabolite. This 'two hit' strategy may offer greater long-term potential through the development of combination therapies that ultimately reduce the risk of emergence of resistance, both through requiring the pathogen to simultaneously acquire resistance to two independent targets, and through the use of lower drug dosages that can result

from increased efficacy (Lehár *et al.*, 2009; Ejim *et al.*, 2011; Spitzer *et al.*, 2011; Aziz *et al.*, 2015).

Of the 909 reactions which were predicted to inhibit growth by less than 50% when knocked out individually, 129 were involved in at least one pair of knockouts that together reduced biomass production to less than 50% (**Figure 7**). Analyses reveal that the model possesses alternative pathways to produce nicotinate—important in redox reactions—and that knocking out different combinations of these pathways had a dramatic impact on biomass production (**Figure 7**; P1, P2, P3, and P11). Our simulations also predict that the loss of one half of the TCA cycle or the other can be compensated for by the model, but not both, and only if the *Wolbachia* TCA cycle is functional (**Figure 7**; P4, P5, P6, and P15). While purine biosynthesis pathways are predicted to be essential by our *in silico* single knockouts, pyrimidine biosynthesis pathways are only predicted as essential through synthetic lethal interactions, suggesting redundancy in these pathways (**Figure 7**; P7, P8, P9, and P10). Finally, we saw evidence of some redundancy in the *B. malayi* pentose phosphate pathways (**Figure 7**; P12 and P13), and observed an interesting nearly lethal interaction between part of the pentose phosphate pathway involved in the metabolism of fructose 6-phosphate and the mitochondrial oxidative phosphorylation reactions (**Figure 7**; P14 and P16).

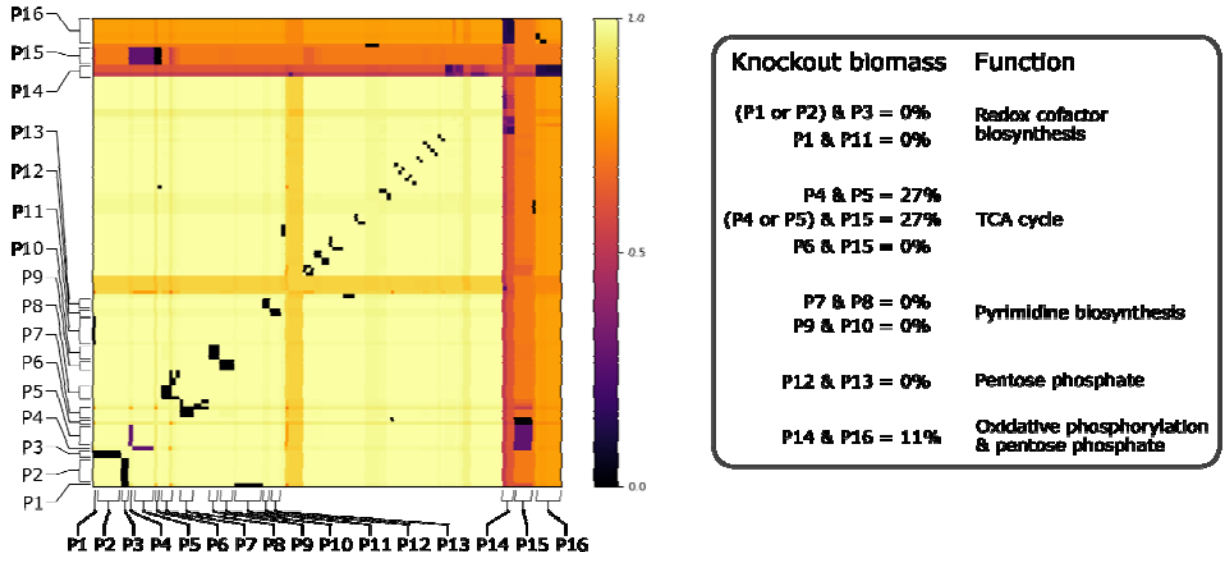

Figure 7. Effects of all double knockouts in the model. This heatmap shows the effect of double knockout combinations of 129 reactions that reduced biomass production below 50%. A value of 1.0 (light yellow) indicates that there was no effect from the knockout, while a value of 0.0 (black) indicates that the model was unable to produce any biomass. Pathways are defined as containing one or more reactions, and 16 of the major pathways are labeled on the heatmap. The legend on the right describes the interactions observed between the pathways.

Fosmidomycin, MDL-29951, and Tenofovir possess antifilarial activity

To validate the performance of our model, we selected a subset of reactions for targeted inhibition using known drugs. Of the 99 reactions predicted to be essential, 77 were associated with one or more genes (33 in the cytosol, 41 in *Wolbachia*, and 3 in the mitochondria). This subset was chosen because they were considered less likely to be model artifacts. Reactions were prioritized by considering their expression across different lifecycle stages, the number and availability of existing inhibitors identified in the ChEMBL database (Gaulton *et al.*, 2012; Davies *et al.*, 2015; Gaulton *et al.*, 2017), and the similarity to human homologs. From this prioritized list we selected three inhibitors to validate our predictions through *in vitro* assays (see **Table 1** for details).

Drug	Predicted target pathway	Developed for	Concentration (µM)
Fosmidomycin	Isoprenoid precursor biosynthesis	Antibiotic/ antimalarial	12.5
MDL-29951	Gluconeogenesis	Epilepsy	12.5
Tenofovir	Purine metabolism	Hepatitis B	12.5

Table 1. Details about the three drugs tested for anti-filarial activity against *B. malayi* adult worms.

As mentioned above, reactions were only prioritized as potential targets if their cognate genes were expressed across the *B. malayi* lifecycle stages (**Table 2**). The predicted Fosmidomycin target, *Wolbachia* gene Wbm0179 (1-deoxy-D-xylulose 5-phosphate reductoisomerase) has moderate expression that is consistent across most stages, high in early adult males but dropping off over time. The target gene of MDL-29951, Bm13850 (fructose biphosphatase), has moderate expression that is highest in L3 but relatively consistent across stages. *Wolbachia* also has a homolog of this gene, Wbm0158, that is expressed at a higher level especially in the late adult stages. Tenofovir was identified as a ChEMBL hit of *B. malayi* Bm9070 (an adenylate kinase), which has very low expression in most stages, but moderate in adult males. There is a *Wolbachia* homolog of this gene as well, Wbm0321, with low expression throughout the life stages. There are two other *B. malayi* genes that are associated with this reaction: Bm3965 (a UMP-CMP kinase) has moderate expression, highest in adult females but quite consistent across stages; and Bm14014 (adenylate kinase isoenzyme 1) has very high expression, highest in L3 but still high in male and female adults.

	Target gene	Life stage expression (FPKM)									
		L3	L3D6	L3D9	L4	F30	F42	F120	M30	M42	M120
Fosmidomycin	Wbm0179	12	17	18	11	27	11	16	37	31	3
MDL-29951	Bm13850	45	21	22	30	22	24	6	31	17	14
	Wbm0158	68	66	69	49	27	40	80	29	40	95
Tenofovir	Bm9070	0	0	0	0	0	1	1	1	4	26
	Wbm0321	34	13	14	4	5	3	15	0	18	6
Tenofovir-associated	Bm3965	18	19	20	11	57	33	14	15	19	17
	Bm14014	419	101	119	105	76	93	21	75	49	32

Table 2. Expression of the predicted drug target genes across *B. malayi* life stages.

These three predicted drug targets were subsequently validated by testing their effects on worms *in vitro*. Fosmidomycin, MDL-29951, and Tenofovir were found to reduce the number of *Wolbachia* per worm by 47% ($p < 0.05$), 76% ($p < 0.001$), and 70% ($p < 0.001$), respectively (**Figure 8**). We also observed two of the drugs impacting fecundity,

512 with Fosmidomycin and Tenofovir reducing the number of microfilariae produced per
513 worm by 33% ($p < 0.01$) and 34% ($p < 0.05$), respectively. Fosmidomycin treatment also
514 appeared to lead to a consistent phenotype affecting motility, but this was not efficiently
515 detected with the Worminator assay (data not shown).

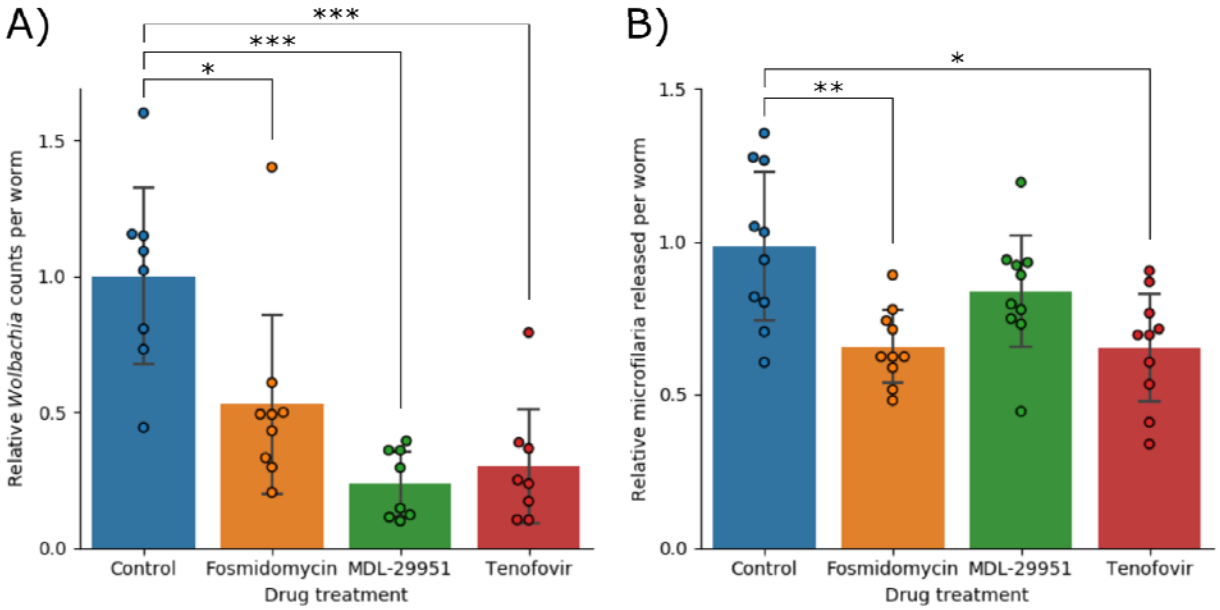

516

517 **Figure 8. Potential anthelmintic activity against adult *B. malayi* worms.** A) shows
518 the number of *Wolbachia* detected per worm, normalized against the control group and
519 B) shows the number of microfilariae released per worm, normalized against the control
520 group. In both data sets significance was detected using a single factor ANOVA,
521 followed by 2-tailed t-tests between each drug and the control with a Bonferroni
522 correction. Error bars indicate the standard deviations; * indicates $p < 0.05$; ** indicates
523 $p < 0.01$; *** indicates $p < 0.001$.

524

525

DISCUSSION

We present the first constraints based metabolic model for *B. malayi*, which we term *i*DC625. While the model captures many known features of nematode metabolism, simulations under a variety of different conditions yielded a number of emergent behaviours, including switching between aerobic and anaerobic metabolic pathways, a predicted Crabtree effect under high oxygen and glucose, and a novel pathway that relies on the catabolism of glutamate to aspartate to generate energy. This suggests that in addition to being robust, the model is capable of generating novel biological hypotheses.

A high quality compartmentalized metabolic model allows us to study the metabolic processes of the cell in detail, including pathways that have been poorly studied in the past; in particular, the anaerobic metabolic pathways used by parasitic nematodes are unlike those studied in most other eukaryotes (Del Borrello *et al.*, 2019). Our model is the first to incorporate this pathway and is therefore likely to yield accurate predictions as low oxygen environments are biologically relevant for parasitic nematodes.

An emergent behaviour predicted by the model was the exhibition of the Crabtree effect, a previously described phenomenon observed in yeast where anaerobic fermentation pathways are activated in aerobic conditions, but only in the presence of high levels of glucose (Postma *et al.*, 1989; Pfeiffer and Morley, 2014). It is interesting to note that succinate export flux mirrors the activity pattern of fumarase (**Figure 3**), potentially indicating that the Crabtree effect occurs only under conditions that result in succinate export. This suggests further investigation of this effect, perhaps through *in vitro* studies of worms exposed to different oxygen and glucose concentrations.

The glyoxylate pathway is primarily discussed in the literature as a way for plants to process fatty acids into glucose and starches, but it is also found in fungi, some protists, and bacteria (Kondrashov *et al.*, 2006). The relevant genes have been detected in several Metazoan species, but the nematodes are the only group where the pathway is widely accepted to be functional, and where it is regarded as a conduit from fatty acids to glucose during embryogenesis. It involves many of the same enzymes as the TCA cycle but includes a “shortcut” from isocitrate to succinate and malate. It has been

556 suggested that this pathway may also play a role in energy metabolism (Butler *et al.*,
557 2012)—in particular when metabolizing fatty acids—and our results appear to support
558 that this hypothesis is plausible.

559 Besides predicting the use of metabolic pathways, our model has the ability to identify
560 reactions essential to growth as potential therapeutic targets. Previous predictions of
561 essentiality based on a compartmentalized model of *C. elegans* metabolism, *i*CEL1273,
562 were broadly consistent with *in vitro* gene essentiality screens (Safak Yilmaz and
563 Walhout, 2016), suggesting the process by which we made our predictions is likely to be
564 biologically relevant.

565 Two of the highly prioritized drug target hits identified in our study were aldolase
566 isozymes *aldo-1* (Bm5580) and *aldo-2* (Bm3135). Knocking out the cognate reactions
567 led to unrecoverable states in the model, both genes have several druggable homologs
568 in ChEMBL, and the expression of both genes was consistent across the adult lifecycle
569 stages (*aldo-1* had the highest stage-specific expression out of any of the prioritized
570 genes). These were not pursued in this work, as in a previous study we examined the
571 effects of knocking down these genes with RNAi in adult female *B. malayi* (Voronin *et*
572 *al.*, 2016). While the knockdown of *aldo-1* had no significant effects, that of *aldo-2*
573 showed effects including a decrease in the *Wolbachia* population, a reduction in
574 fecundity of female worms, and an increase in apoptotic embryos. This shows that our
575 model is capable of predicting viable targets in the adult worms.

576 We validated our predictions of essential reactions by observing the effects of three
577 existing drugs on *B. malayi* adults. Fosmidomycin was originally investigated as an
578 antibiotic in the 1980s, but more recently has been studied as an anti-malarial drug
579 (Umeda *et al.*, 2011; Jomaa *et al.*, 1999; Armstrong *et al.*, 2015). It acts on the non-
580 mevalonate isoprenoid biosynthesis pathway, which is generally only found in some
581 bacteria and plants, in addition to the apicoplast of *Plasmodium falciparum*. This helps
582 to contribute to the drug's excellent safety profile. Tenofovir is currently licensed by the
583 FDA for treatment of HIV and Hepatitis B (Agarwal *et al.*, 2015). It is used as a
584 nucleoside reverse transcriptase inhibitor, and its action against *B. malayi* may work by
585 a similar mechanism, by competitive inhibition with AMP of adenylate kinase. MDL-

586 29951 was identified as an inhibitor of fructose 1,6-bisphosphatase as a potential
587 treatment for diabetes (Wright *et al.*, 2003). Interestingly, this enzyme has recently and
588 independently been proposed as a drug target against *Leishmania* species (Yuan *et al.*,
589 2017). That study also solved several crystal structures of the enzyme, which would
590 prove valuable for future refinements of the drug. There have also been several other
591 inhibitors generated and tested against this enzyme from different species, which could
592 provide a rich starting point for future work to refine the antiparasitic activity (Dang *et al.*,
593 2009, 2010; Tsukada *et al.*, 2010; Kaur *et al.*, 2017). Both Tenofovir and MDL-29951
594 were expected to act against *B. malayi*, but primarily resulted in a significant reduction
595 of *Wolbachia* populations when tested. The mechanism of action of these drugs against
596 the endosymbiont is unclear, but *Wolbachia* does possess a homolog of both drug
597 targets—(Wbm0321 (adenylate kinase) for Tenofivir; Wbm0158 (fructose-1,6-
598 biphosphatase) for MDL-29951)—that the drugs may be acting against.

599 All three of the drugs tested in this study appear to possess activity against adult *B.*
600 *malayi* worms, via reduction in *Wolbachia* populations and/or microfilaria production.
601 The successful validation of these effects suggests that our metabolic model is a useful
602 approximation of the worm. Further research on this model may therefore yield even
603 more therapeutic targets.

604

MATERIALS AND METHODS

Metabolic reconstruction and flux balance analyses

An initial metabolic reconstruction was generated as described in (Cotton *et al.*, 2016). Briefly, sets of metabolic enzymes were identified from the *B. malayi* gene models using DETECT V2 (Hung *et al.*, 2010), BLASTP (Camacho *et al.*, 2009) searches against enzymes curated in the SWISSPROT database (Bateman *et al.*, 2015), PRIAM (Claudel-Renard *et al.*, 2003), EFICAz (Tian *et al.*, 2004), and the BRENDA database (Schomburg *et al.*, 2002). Assignment of metabolic pathways and gap-filling in the reconstruction were performed by Pathway Tools (Karp *et al.*, 2016).

All network analysis methods, including FBA, were performed using the cobrapy package version 0.5.10 (Ebrahim *et al.*, 2013), which is a Python-based implementation of the popular COBRA toolbox of FBA-associated methods (Schellenberger *et al.*, 2011). One drawback of FBA is that there are usually many different sets of reaction fluxes that can lead to the same solution, with no accepted way to choose the most biologically relevant. Parsimonious FBA (pFBA) is a permutation of this algorithm that first maximizes the objective function, and then identifies the solution with the smallest sum over all reaction fluxes. This is predicted to yield more biologically relevant solutions, and helps to ensure that analyses of the model under different conditions are likely to yield comparable sets of reaction fluxes.

Generation of transcriptomic data for the *Wolbachia* endosymbiont during molting

Previously published transcriptome data was used for this study, with the exception of the *Wolbachia* trascriptome during the molting of the worm from L3, L3 day 6, and L3 day 9. These data were generated as described in (Grote *et al.*, 2019). In brief, all *B. malayi* worms were obtained from FR3 (Filariasis Research Reagent Resource Center; BEI Resources, Manassas, VA, USA). Infective third-stage larvae (iL3) were recovered

633 from mosquitoes (*Aedes aegypti*) and mammalian stage larvae were recovered from
634 gerbils (*Meriones unguiculatus*) at 6 and 9 days post infection (dpi). Total RNA was
635 prepared from *B. malayi* worms and *Wolbachia* as previously described (Grote *et al.*,
636 2017). RNA was prepared from 3 biological replicates of infective L3 (iL3; 2000 larvae
637 each), 3 replicates of 6 dpi larvae (1500 each) and 2 replicates of 9 dpi larvae (1300
638 each). Libraries were prepared using the NEBNext Ultra II RNA Library Prep Kit for
639 Illumina (New England Biolabs) according to manufacturer instructions. Libraries were
640 sequenced at NYU's GenCore on the Illumina NextSeq500 platform with 150bp paired-
641 end reads. Sequence reads from each sample were analyzed with the Tuxedo suite of
642 tools (Trapnell *et al.*, 2010, 2013; Kim *et al.*, 2013). Reads were mapped with Tophat2's
643 Bowtie2-very-sensitive algorithm to the genome assembly of *Wolbachia* of *B. malayi*
644 (Foster *et al.*, 2005). Each biological replicate received an average of 1.3 million reads
645 that mapped to the *Wolbachia* genome. The resulting BAM files were then used with
646 HtSeq to obtain raw read counts. Differential gene expression analysis was performed
647 using EdgeR (Robinson *et al.*, 2010), Data was combined with previously published
648 stages 16 dpi (L4), and male and female worms at 30, 42 and 120 dpi (Grote *et al.*,
649 2017).

650

651 **Generation of lifecycle stage specific metabolic models**

652 To understand how metabolic pathway dependencies may vary across the *B. malayi*
653 lifecycle, we integrated new and existing stage-specific RNA-Seq datasets to generate
654 lifecycle stage specific metabolic models. Of the 849 enzymatic reactions in the model
655 with gene evidence, 837 had stage-specific expression data, allowing constraints to be
656 placed on their associated metabolic flux. RNA-Seq enzyme expression was used to
657 apply constraints on reaction flux as we have done previously (Song *et al.*, 2013). In
658 brief, the expression of each gene was normalized across lifecycle stages, and the
659 relative expression for each stage was applied to the upper and lower bounds of all
660 associated reactions. For example, if the expression of a gene in one particular lifecycle
661 stage was measured to be 30% of its maximum across all stages, the corresponding
662 lower and upper reaction bounds for that life stage model would be set to (0, 300) or (-

300, 300) in arbitrary flux units, for irreversible and reversible reactions, respectively; the default bounds are (0, 1000) or (-1000, 1000) for irreversible and reversible reactions, respectively. As we cannot determine whether a measured expression of zero indicates no expression or that the transcripts were simply not sequenced, all reactions with a measured expression of zero were left unconstrained in the model. This yielded 11 distinct metabolic models: open or unconstrained (i.e. without any expression constraints), L3, L3D6, L3D9, L4, F30, F42, F120, M30, M42, and M120; where L3D6 indicates worms in the 3rd larval stage 6 days post-infection, and F30 and M30 indicate adult female and male worms 30 days post-infection, respectively.

Metabolomics sample preparation and run

All parasites were obtained from FR3 (Filariasis Research Reagent Resource Center; BEI Resources, Manassas, VA, USA) where they were isolated and separated by sex from infected gerbils (*Meriones unguiculatus*) or mosquitoes (*Aedes aegypti*). Worms were flash-frozen and shipped to the New York Blood Center for processing. Stages used for metabolomics analysis included L3 larvae from mosquitoes, adult male and female worms at 120dpi, and microfilaria. The number of worms per sample were 20 adult female worms, 40 adult males, 2X10^{6} microfilariae, and 200 L3 larvae per biological replicate. Samples were washed in 1x PBS and run in triplicate. Adult male and female worms were picked individually from PBS and each biological was weighed. The microfilaria and L3 samples were spun down, the PBS pipetted off, and weighed directly into a metabolomics 2mL screw cap vial with total amounts ranging from 1.3 mg (adult males) to 15.8 mg (microfilaria). Metabolites were extracted and the data analyzed as described in the Supplementary Information.

Validation of drug targets

For validation, 15 adult female and 15 adult male worms (120 dpi) were cultured *in vitro* for each drug treatment or control group. Worms were cultured for six days in a 12-well plate with 2 worms per well, in complete culture medium (RPMI-1640 supplemented

with 10% FBS, 100 U/mL penicillin, 100 mg/mL streptomycin, 2 mM L-glutamine) at 37°C under 5% CO_2. Three drugs were assayed: Fosmidomycin, MDL-29951, and Tenofovir, each at a concentration of 12 µM. Media was changed every other day.

Microfilarial release by female worms was determined by quantifying the number present in the media on the 6th day of treatment and collection of adult worms. Two technical replicates and 10 biological replicates were used to determine microfilaria production. Significance was determined by a single factor ANOVA, followed by t-tests between each treatment group and the control using a Bonferroni correction.

To analyze the number of *Wolbachia* per worm, DNA was extracted from adult male worms using the QIAmp DNA Mini Kit (QIAGEN) according to the manufacturer's protocol. *Wolbachia* per individual worm was calculated by genomic qPCR using primers for a single-copy *Wolbachia* gene (*wsp*; accession AAW71020). Each treatment or control group had 8 (or 9) biological replicates, and each replicate contained 3 male worms. Significance was determined by a single factor ANOVA, followed by t-tests between each treatment group and the control using a Bonferroni correction.

The Worminator system (Storey *et al.*, 2014) was used to assess changes in motility upon drug treatment. Motility of adult female worms was assessed using one female worm per well in a 12 well plate. Each treatment or control had 8 biological replicates.

DATA AVAILABILITY

All of our metabolic models–the unconstrained and lifecycle stage-specific variants–are freely available at https://github.com/ParkinsonLab/Brugia_metabolic_network.

Transcriptomics data generated for the *B. malayi* molt (lifecycle stages L3 to L3D6 to L3D9) are available through the Sequence Read Archive (PRJNA557263). Other transcriptomics data used in this study are also available through the Sequence Read Archive (SRP090644).

All of our metabolomics data – from both the hybrid and predictive analyses – are freely available at https://github.com/ParkinsonLab/Brugia_metabolic_network.

720

721 **ACKNOWLEDGEMENTS**

722 This research was supported by a grant to JP and EG from the National Institutes of
723 Health (R21AI126466). Additional sources of funding include the Natural Sciences and
724 Engineering Research Council to JP (NSERC; RGPIN-2014-06664). NN was supported
725 by a student Restracomp fellowship given by the Hospital for Sick Children. Funding for
726 AG was provided by the T32 Ruth L. Kirschstein Institutional National Research Service
727 Award (T32AI007180) and the F31 Ruth L. Kirschstein Pre-doctoral Individual NRSA
728 (F31AI131527). Worms for this study were provided by FR3 (Filariasis Research
729 Reagent Resource Center; BEI Resources, Manassas, VA, USA). New York
730 University's Genomics Core (GenCore) is supported by the Zegar Family Foundation.

REFERENCES

Agarwal,K. *et al.* (2015) Twenty-eight day safety, antiviral activity, and pharmacokinetics of tenofovir alafenamide for treatment of chronic hepatitis B infection. *J. Hepatol.*, **62**, 533–540.

Aljayyoussi,G. *et al.* (2017) Short-course, high-dose rifampicin achieves Wolbachia depletion predictive of curative outcomes in preclinical models of lymphatic filariasis and onchocerciasis. *Sci. Rep.*, **7**.

Armstrong,C.M. *et al.* (2015) Resistance to the antimicrobial agent fosmidomycin and an FR900098 prodrug through mutations in the deoxyxylulose phosphate reductoisomerase gene (dxr). *Antimicrob. Agents Chemother.*, **59**, 5511–5519.

Awadzi,K. *et al.* (2004) An investigation of persistent microfilaridermias despite multiple treatments with ivermectin, in two onchocerciasis-endemic foci in Ghana. *Ann. Trop. Med. Parasitol.*, **98**, 231–249.

Aziz,R.K. *et al.* (2015) Systems biology-guided identification of synthetic lethal gene pairs and its potential use to discover antibiotic combinations. *Sci. Rep.*, **5**.

Bakker,B.M. *et al.* (2001) Stoichiometry and compartmentation of NADH metabolism in Saccharomyces cerevisiae. In, *FEMS Microbiology Reviews*., pp. 15–37.

Bateman,A. *et al.* (2015) UniProt: A hub for protein information. *Nucleic Acids Res.*

Berg,J. *et al.* (2002) Biochemistry.

Del Borrello,S. *et al.* (2019) Rhodoquinone biosynthesis in C. elegans requires precursors generated by the kynurenine pathway. *Elife*.

Boussinesq,M. *et al.* (1998) Three probable cases of LOA loa encephalopathy following ivermectin treatment for onchocerciasis. *Am. J. Trop. Med. Hyg.*, **58**, 461–469.

Boussinesq,M. *et al.* (2006) What are the mechanisms associated with post-ivermectin serious adverse events? *Trends Parasitol.*, **22**, 244–246.

Bremer,J. and Davis,E.J. (1975) Studies on the active transfer of reducing equivalents into mitochondria via the malate-aspartate shuttle. *BBA - Bioenerg.*, **376**, 387–397.

758 Butler,J.A. *et al.* (2012) Profiling the Anaerobic Response of C. elegans Using GC-MS.
759 *PLoS One*, **7**.

760 Camacho,C. *et al.* (2009) BLAST+: Architecture and applications. *BMC Bioinformatics*,
761 **10**, 1.

762 Chavali,A.K. *et al.* (2008) Systems analysis of metabolism in the pathogenic
763 trypanosomatid Leishmania major. *Mol. Syst. Biol.*, **4**, 177.

764 Chen,W.W. *et al.* (2016) Absolute Quantification of Matrix Metabolites Reveals the
765 Dynamics of Mitochondrial Metabolism. *Cell*.

766 Chiappino-Pepe,A. *et al.* (2017) Bioenergetics-based modeling of Plasmodium
767 falciparum metabolism reveals its essential genes, nutritional requirements, and
768 thermodynamic bottlenecks. *PLoS Comput. Biol.*

769 Claudel-Renard,C. *et al.* (2003) Enzyme-specific profiles for genome annotation:
770 PRIAM. *Nucleic Acids Res.*

771 Cotton,J.A. *et al.* (2016) The genome of Onchocerca volvulus, agent of river blindness.
772 *Nat. Microbiol.*, **2**, 16216.

773 Dang,Q. *et al.* (2009) Fructose-1,6-bisphosphatase inhibitors. 1. Purine phosphonic
774 acids as novel AMP mimics. *J. Med. Chem.*, **52**, 2880–2898.

775 Dang,Q. *et al.* (2010) Fructose-1,6-bisphosphatase inhibitors. 2. Design, synthesis, and
776 structure-activity relationship of a series of phosphonic acid containing
777 benzimidazoles that function as 5′-adenosinemonophosphate (AMP) mimics. *J.*
778 *Med. Chem.*, **53**, 441–451.

779 Darby,A.C. *et al.* (2012) Analysis of gene expression from the Wolbachia genome of a
780 filarial nematode supports both metabolic and defensive roles within the symbiosis.
781 *Genome Res.*, **22**, 2467–2477.

782 Davies,M. *et al.* (2015) ChEMBL web services: Streamlining access to drug discovery
783 data and utilities. *Nucleic Acids Res.*, **43**, W612–W620.

784 Debrah,A.Y. *et al.* (2009) Reduction in levels of plasma vascular endothelial growth

785 factor-A and improvement in hydrocele patients by targeting endosymbiotic
786 Wolbachia sp. in Wuchereria bancrofti with doxycycline. *Am. J. Trop. Med. Hyg.*,
787 **80**, 956–963.

788 Eberhard,M.L. *et al.* (1991) Evidence of nonsusceptibility to diethylcarbamazine in
789 wucheria bancrofti. *J. Infect. Dis.*, **163**, 1157–1160.

790 Ebrahim,A. *et al.* (2013) COBRApy: COnstraints-Based Reconstruction and Analysis for
791 Python. *BMC Syst. Biol.*, **7**, 74.

792 Ejim,L. *et al.* (2011) Combinations of antibiotics and nonantibiotic drugs enhance
793 antimicrobial efficacy. *Nat. Chem. Biol.*, **7**, 348–350.

794 Eng,J.K.L. *et al.* (2006) Ivermectin selection on β-tubulin: Evidence in Onchocerca
795 volvulus and Haemonchus contortus. *Mol. Biochem. Parasitol.*, **150**, 229–235.

796 Foster,J. *et al.* (2005) The Wolbachia genome of Brugia malayi: Endosymbiont evolution
797 within a human pathogenic nematode. *PLoS Biol.*, **3**, 0599–0614.

798 Gardon,J. *et al.* (1997) Serious reactions after mass treatment of onchocerciasis with
799 ivermectin in an area endemic for Loa loa infection. *Lancet*, **350**, 18–22.

800 Gaulton,A. *et al.* (2012) ChEMBL: A large-scale bioactivity database for drug discovery.
801 *Nucleic Acids Res.*, **40**.

802 Gaulton,A. *et al.* (2017) The ChEMBL database in 2017. *Nucleic Acids Res.*, **45**, D945–
803 D954.

804 Ghedin,E. *et al.* (2009) Brugia malayi gene expression in response to the targeting of
805 the Wolbachia endosymbiont by tetracycline treatment. *PLoS Negl. Trop. Dis.*, **3**.

806 Ghedin,E. *et al.* (2007) Draft genome of the filarial nematode parasite Brugia malayi.
807 *Science (80-.).*, **317**, 1756–1760.

808 Gleave,K. *et al.* (2016) Filarial infection influences mosquito behaviour and fecundity.
809 *Sci. Rep.*

810 Grote,A. *et al.* (2017) Defining Brugia malayi and Wolbachia symbiosis by stage-specific
811 dual RNA-seq. *PLoS Negl. Trop. Dis.*, **11**.

812 Grote,A. *et al.* (2019) Prediction pipeline for discovery of regulatory motifs associated
813 with Brugia malayi molting. *Submitted*.

814 Gyapong,J.O. *et al.* (2005) Treatment strategies underpinning the global programme to
815 eliminate lymphatic filariasis. *Expert Opin. Pharmacother.*, **6**, 179–200.

816 Hung,S.S. *et al.* (2010) DETECT-a density estimation tool for enzyme classification and
817 its application to Plasmodium falciparum. *Bioinformatics*.

818 Jomaa,H. *et al.* (1999) Inhibitors of the nonmevalonate pathway of isoprenoid
819 biosynthesis as antimalarial drugs. *Science (80-.).*, **285**, 1573–1576.

820 Kaplan,R.M. and Vidyashankar,A.N. (2012) An inconvenient truth: Global worming and
821 anthelmintic resistance. *Vet. Parasitol.*, **186**, 70–78.

822 Karp,P.D. *et al.* (2016) Pathway tools version 19.0 update: Software for
823 pathway/genome informatics and systems biology. *Brief. Bioinform.*

824 Kaur,R. *et al.* (2017) Fructose-1,6-bisphosphatase inhibitors: A new valid approach for
825 management of type 2 diabetes mellitus. *Eur. J. Med. Chem.*, **141**, 473–505.

826 Kim,D. *et al.* (2013) TopHat2: Accurate alignment of transcriptomes in the presence of
827 insertions, deletions and gene fusions. *Genome Biol.*, **14**.

828 Kondrashov,F.A. *et al.* (2006) Evolution of glyoxylate cycle enzymes in Metazoa:
829 Evidence of multiple horizontal transfer events and pseudogene formation. *Biol.*
830 *Direct*, **1**.

831 Lee,D.S. *et al.* (2009) Comparative genome-scale metabolic reconstruction and flux
832 balance analysis of multiple Staphylococcus aureus genomes identify novel
833 antimicrobial drug targets. *J. Bacteriol.*, **191**, 4015–4024.

834 Lehár,J. *et al.* (2009) Synergistic drug combinations tend to improve therapeutically
835 relevant selectivity. *Nat. Biotechnol.*, **27**, 659–666.

836 Li,B.W. *et al.* (2009) Transcriptomes and pathways associated with infectivity, survival
837 and immunogenicity in Brugia malayi L3. *BMC Genomics*.

838 Molyneux,D.H. *et al.* (2014) Multidimensional complexities of filariasis control in an era

839 of large-scale mass drug administration programmes: A can of worms. *Parasites*
840 *and Vectors*, **7**.

841 Muller,M. *et al.* (2012) Biochemistry and Evolution of Anaerobic Energy Metabolism in
842 Eukaryotes. *Microbiol. Mol. Biol. Rev.*, **76**, 444–495.

843 Oberhardt,M.A. *et al.* (2008) Genome-scale metabolic network analysis of the
844 opportunistic pathogen Pseudomonas aeruginosa PAO1. *J. Bacteriol.*, **190**, 2790–
845 2803.

846 Orth,J.D. *et al.* (2010) What is flux balance analysis? *Nat. Biotechnol.*, **28**, 245–248.

847 Pfeiffer,T. and Morley,A. (2014) An evolutionary perspective on the Crabtree effect.
848 *Front. Mol. Biosci.*, **1**.

849 Postma,E. *et al.* (1989) Enzymic analysis of the crabtree effect in glucose-limited
850 chemostat cultures of Saccharomyces cerevisiae. *Appl. Environ. Microbiol.*, **55**,
851 468–477.

852 Rao,R.U. *et al.* (2012) Effects of Doxycycline on gene expression in Wolbachia and
853 Brugia malayi adult female worms in vivo. *J. Biomed. Sci.*, **19**.

854 Robinson,M.D. *et al.* (2010) edgeR: a Bioconductor package for differential expression
855 analysis of digital gene expression data. *Bioinformatics*, **26**.

856 Safak Yilmaz,L. and Walhout,A.J.M. (2016) A Caenorhabditis elegans Genome-Scale
857 Metabolic Network Model. *Cell Syst.*, **2**, 297–311.

858 Schellenberger,J. *et al.* (2011) Quantitative prediction of cellular metabolism with
859 constraint-based models: The COBRA Toolbox v2.0. *Nat. Protoc.*, **6**, 1290–1307.

860 Schomburg,I. *et al.* (2002) BRENDA: A resource for enzyme data and metabolic
861 information. *Trends Biochem. Sci.*

862 Schwab,A.E. *et al.* (2005) Detection of benzimidazole resistance-associated mutations
863 in the filarial nematode Wuchereria bancrofti and evidence for selection by
864 albendazole and ivermectin combination treatment. *Am. J. Trop. Med. Hyg.*, **73**,
865 234–238.

866 Simón-Manso,Y. *et al.* (2013) Metabolite profiling of a NIST standard reference material
867 for human plasma (SRM 1950): GC-MS, LC-MS, NMR, and clinical laboratory
868 analyses, libraries, and web-based resources. *Anal. Chem.*

869 Smith,C.A. *et al.* (2005) METLIN: A metabolite mass spectral database. In, *Therapeutic*
870 *Drug Monitoring*.

871 Song,C. *et al.* (2013) Metabolic reconstruction identifies strain-specific regulation of
872 virulence in Toxoplasma gondii. *Mol. Syst. Biol.*, **9**.

873 Spitzer,M. *et al.* (2011) Cross-species discovery of syncretic drug combinations that
874 potentiate the antifungal fluconazole. *Mol. Syst. Biol.*, **7**.

875 Storey,B. *et al.* (2014) Utilization of computer processed high definition video imaging
876 for measuring motility of microscopic nematode stages on a quantitative scale: 'The
877 Worminator'. *Int. J. Parasitol. Drugs Drug Resist.*, **4**, 233–243.

878 Taylor,M.J. *et al.* (2010) Lymphatic filariasis and onchocerciasis. In, *The Lancet*., pp.
879 1175–1185.

880 Taylor,M.J. *et al.* (2019) Preclinical development of an oral anti-Wolbachia macrolide
881 drug for the treatment of lymphatic filariasis and onchocerciasis. *Sci. Transl. Med.*

882 Taylor,M.J. *et al.* (2013) Wolbachia filarial interactions. *Cell. Microbiol.*, **15**, 520–526.

883 Tian,W. *et al.* (2004) EFICAz: A comprehensive approach for accurate genome-scale
884 enzyme function inference. *Nucleic Acids Res.*

885 Tielens,A.G.M. *et al.* (2010) Acetate formation in the energy metabolism of parasitic
886 helminths and protists. *Int. J. Parasitol.*, **40**, 387–397.

887 Trapnell,C. *et al.* (2013) Differential analysis of gene regulation at transcript resolution
888 with RNA-seq. *Nat. Biotechnol.*, **31**, 46–53.

889 Trapnell,C. *et al.* (2010) Transcript assembly and quantification by RNA-Seq reveals
890 unannotated transcripts and isoform switching during cell differentiation. *Nat.*
891 *Biotechnol.*, **28**, 511–515.

892 Tsukada,T. *et al.* (2010) Structure-based drug design of tricyclic 8H-indeno[1,2-

d][1,3]thiazoles as potent FBPase inhibitors. *Bioorganic Med. Chem. Lett.*, **20**, 1004–1007.

Umeda,T. *et al.* (2011) Molecular basis of fosmidomycin's action on the human malaria parasite Plasmodium falciparum. *Sci. Rep.*, **1**.

Voronin,D. *et al.* (2016) Glucose and glycogen metabolism in brugia malayi is associated with wolbachia symbiont fitness. *PLoS One*, **11**.

Vos,T. *et al.* (2016) Global, regional, and national incidence, prevalence, and years lived with disability for 310 diseases and injuries, 1990–2015: a systematic analysis for the Global Burden of Disease Study 2015. *Lancet*, **388**, 1545–1602.

Wright,S.W. *et al.* (2003) 3-(2-Carboxy-ethyl)-4,6-dichloro-1H-indole-2-carboxylic acid: An allosteric inhibitor of fructose-1,6-bisphosphatase at the AMP site. *Bioorganic Med. Chem. Lett.*, **13**, 2055–2058.

Yuan,M. *et al.* (2017) Structures of Leishmania Fructose-1,6-Bisphosphatase Reveal Species-Specific Differences in the Mechanism of Allosteric Inhibition. *J. Mol. Biol.*, **429**, 3075–3089.